Magic-angle magnonic nanocavity in a magnetic moiré superlattice

Jilei Chen,[1,2,3] Lang Zeng,[2] Hanchen Wang,[2] Marco Madami,[4] Gianluca Gubbiotti,[5] Song Liu,[1,3] Jianyu Zhang,[2] Zifeng Wang,[2] Wenhao Jiang,[6] Yan Zhang,[6] Dapeng Yu,[1,3] Jean-Philippe Ansermet,[7,1] and Haiming Yu[2,1,3,*]

[1]*Shenzhen Institute for Quantum Science and Engineering (SIQSE), Southern University of Science and Technology, Shenzhen, People's Republic of China*

[2]*Fert Beijing Institute, MIIT Key Laboratory of Spintronics, School of Integrated Circuit Science and Engineering, Beihang University, Beijing 100191, People's Republic of China*

[3]*International Quantum Academy, Shenzhen 518048, Peoples Republic of China*

[4]*Dipartimento di Fisica e Geologia, Università di Perugia, Perugia I-06123, Italy*

[5]*Istituto Officina dei Materiali del Consiglio Nazionale delle Ricerche (IOM-CNR), c/o Dipartimento di Fisica e Geologia, Perugia I-06123, Italy*

[6]*School of Electronic and Information Engineering, Beihang University, Xueyuan Road 37, Beijing 100191, People's Republic of China*

[7]*Institute of Physics, Ecole Polytechnique Fédérale de Lausanne (EPFL), 1015 Lausanne, Switzerland*

(Received 10 November 2021; revised 2 March 2022; accepted 7 March 2022; published 31 March 2022)

Moiré superlattices have recently been extensively studied in both electronic and photonic systems, e.g., magic-angle bilayer graphene showing superconductivity and twisted bilayer photonic crystals leading to magic-angle lasers. However, the moiré physics is barely studied in the field of magnonics, i.e., in using spin waves for information processing. In this work, we report magnon flat-band formation in twisted bilayer magnonic crystals at the optimal "magic angle" and interlayer exchange coupling combination using micromagnetic simulations. At the flat-band frequency, magnons undergo a strong two-dimensional confinement with a lateral scale of about 185 nm. The magic-angle magnonic nanocavity occurs at the *AB* stacking region of a moiré unit cell, unlike its photonic counterpart which is at the *AA* region, due to the exchange-induced magnon spin torque. The magnon flat band originates from band structure reformation induced by interlayer magnon-magnon coupling. Our results enable efficient accumulation of magnon intensity in a confined region that is key for potential applications such as magnon Bose-Einstein condensation and even magnon lasing.

DOI: 10.1103/PhysRevB.105.094445

I. INTRODUCTION

Two layers of two-dimensional (2D) lattices placed on top of one another with a small twist angle can generate a new periodicity much larger than the original lattice constant, referred to as a "moiré superlattice." Moiré superlattices of 2D materials, such as twisted bilayer graphene [1–9], are found to exhibit superconductivity [10] and correlated insulator states [11], and therefore have attracted tremendous interest in the emerging field of twistronics based on van der Waals layered materials. At the "magic angle" of approximately 1.1° of the moiré superlattices, the Fermi velocity turns to zero and the energy band near the Fermi level becomes flat in twisted bilayer graphene leading to exotic electronic states. The concept of twistronics is also applied in photonics, where twisted bilayer photonic crystals [12–14] show flat bands at small magic angles resulting in highly localized photonic modes with potential applications such as Bose-Einstein condensation. Magnons, the quanta of spin waves (SWs), being also bosons, are the collective excitation of electron spins in magnetic materials and are intensively investigated in the perspective of magnonics or magnon spintronics [15–22], using magnons as information carriers in low-power-consumption spintronic devices [23,24]. Magnonic crystals [25–30] are the magnetic counterpart of photonic crystals. The magnon transport can be modulated by tuning the SW band gaps [31,32] with novel functions such as reconfigurability [33–35] and nonreciprocity [36–39]. Recently, Gallardo *et al.* [40] have proposed to pattern arrays of heavy-metal wires to impose periodical Dzyaloshinskii-Moriya interaction (DMI) on magnetic thin films. The simulations predict the emergence of flat bands in the bicomponent magnonic crystals with large DMI values. The heavy metal needed for the DMI [41] may severely affect the magnetic damping [42] and thus hinders its practical applications. Recent theoretical works report novel magnon behavior in twisted bilayer magnets in the presence of the DMI [43,44] and stacking domain walls [45]. However, the magnons studied in these works are at extremely high frequencies (energy), making them difficult for practical applications in coherent magnonics operating typically at GHz frequencies [22]. Up to now, magnon flat bands and magnonic nanocavities in moiré magnonic-crystal systems have not been reported.

*haiming.yu@buaa.edu.cn

In this paper, we report magnon flat bands formed in magnetic moiré superlattices by stacking two square antidot lattices with a finite twist angle (referred as "magic angle"). The results from micromagnetic simulations reveal that the perfect flat band emerges at an optimal combination of the "magic angle" and interlayer exchange coupling, and covers almost half of the first magnonic Brillouin zone (BZ) in the reciprocal space. Due to zero group velocity and high density of states of magnons at the flat-band frequency, a highly localized SW mode, i.e., magnonic nanocavity, is discovered at the center of one moiré unit cell with *AB* bilayer stacking. This is analogous to, but fundamentally different from, the recently discovered magic-angle photonic nanocavity [14] occurring always at the *AA* stacking region of moiré photonic superlattices. The emergence of the magnon flat band is attributed to the lowest band formed by the mode anticrossings in the SW dispersion due to interlayer magnon-magnon coupling [46–49]. The magic-angle magnonic nanocavity possesses a quality factor approximately two orders of magnitude higher than that of the non-flat-band mode, and exhibits a narrow spatial linewidth of about 185 nm inversely associated with the flat-band wave vector bandwidth.

II. RESULTS AND DISCUSSION

The magnetic moiré superlattice considered in this work is depicted in Fig. 1(a), which consists of two identical yttrium iron garnet (YIG) layers twisted by an angle θ. YIG thin films with low magnetic damping [50,51] have recently been achieved and demonstrated experimentally for coherent magnonics. The saturation magnetization, intralayer exchange, and magnetic damping are set as $M_S = 140$ kA/m, $A_{11} = 3.7 \times 10^{-12}$ J/m, and $\alpha = 0.0001$, respectively [52]. Each YIG layer is patterned into an antidot square lattice [13,25] with a periodicity of $a_0 = 100$ nm and an antidot diameter of $d = 50$ nm, which can be fabricated with cutting-edge nanotechnology [20,53]. The thickness of a single layer is set as 2 nm. Two layers are separated by 2 nm and coupled with the interlayer exchange A_{12}. By rotating one layer with respect to the other, a moiré superlattice is then formed as shown in Fig. 1(a). The moiré lattice constant can be estimated using $a_m = a_0/\theta$ [12], where a_0 is the lattice constant of a single-layer magnonic crystal being 100 nm. With $\theta = 3.5°$, the moiré lattice constant is estimated to be approximately 1.6 μm. A moiré unit cell is then a 1.6 μm $\times$ 1.6 μm region, e.g., the black dotted square (with *AA* stacking region at the center) or the white dashed square (with *AB* stacking region at the center) in Fig. 1(a). In this work, we take the white region as the moiré unit cell. The simulated structure covers an area of 6 μm $\times$ 6 μm in the *xy* plane with a cell size of 5 nm $\times$ 5 nm. A sinusoidal microwave pulse is applied in the middle of the investigated structure with a width of 20 nm in the *x* direction for obtaining the full SW dispersion spectra, mimicking a nano-stripline in experiments [54]. The excited magnon wave vector then points along the *x* direction. A magnetic field of 50 mT is applied along the *y* axis, so the Damon-Eshbach SW configuration [55,56] is investigated.

Figure 1(b) shows the SW dispersion from the micromagnetic simulation [61] performed at the center of the moiré unit cell [white dashed square in Fig. 1(a)]. Here, we set the

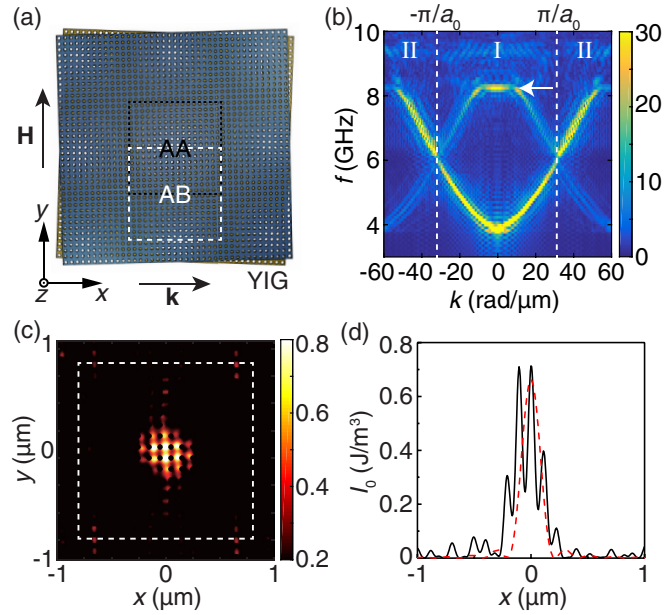

FIG. 1. (a) Schematic illustration of a YIG-based magnetic moiré superlattice with a twist angle of $\theta = 3.5°$. The white dashed (black dotted) square represents the moiré unit cell with *AB* (*AA*) stacking region at its center. A magnetic field of 50 mT is applied in the *y* direction. (b) SW dispersion obtained from micromagnetic simulations with the interlayer exchange coupling of $A_{12} = 11$ μJ/m^2. The white dashed lines represent the BZ boundaries, which define the first BZ ("I") and second BZ ("II"). (c) The spatial distribution of the magnetization dynamics (m_x in the bottom layer) at $t = 4.3$ ns with *AB* stacking after the start of continuous excitation. One moiré unit cell is indicated by the white dashed square being the same white dashed region marked in (a). A magnonic nanocavity is formed at its center (*AB* stacking region). A line-cut of the magnon intensity at $y = 0$ is presented in (d), where the calculation by Eq. (3) (red dashed curve) yields a linewidth of 185 nm.

twist angle $\theta = 3.5°$ and the interlayer exchange coupling $A_{12} = 11$ μJ/m^2, which is about two orders of magnitude weaker than the Ruderman-Kittel-Kasuya-Yosida exchange interaction in metallic spin valves [57,58], one order of magnitude weaker than those at YIG/Co [46] and YIG/Py [59] interfaces, and comparable with that in YIG/Au/YIG magnon valves [60]. The interlayer dipolar interaction is also included in the micromagnetic simulations based on OOMMF [61]. The excitation microwave power is set to be -10 dBm to be maintained in the linear regime. The OOMMF is a finite-difference micromagnetic solver. It was used to model the YIG-based artificial moiré superlattice which has dimensions much larger than the atomic scale. The two-dimensional Fourier transformation is performed on dynamic magnetization components in order to obtain the magnonic band structure. Compared with a single-layer magnonic crystal (see Supplemental Material [62]), an unexpected flat band appears at around 8.2 GHz marked by the white arrow in Fig. 1(b). The magnonic flat band covers a broad wave vector range from -15 rad/μm to 15 rad/μm, which is about half of the first BZ of the magnonic crystal marked as "I" in Fig. 1(b) with BZ boundaries (white dashed lines) at ± 31.4 rad/μm corresponding to $\pm\pi/a_0$. The flat band locates around $k = 0$

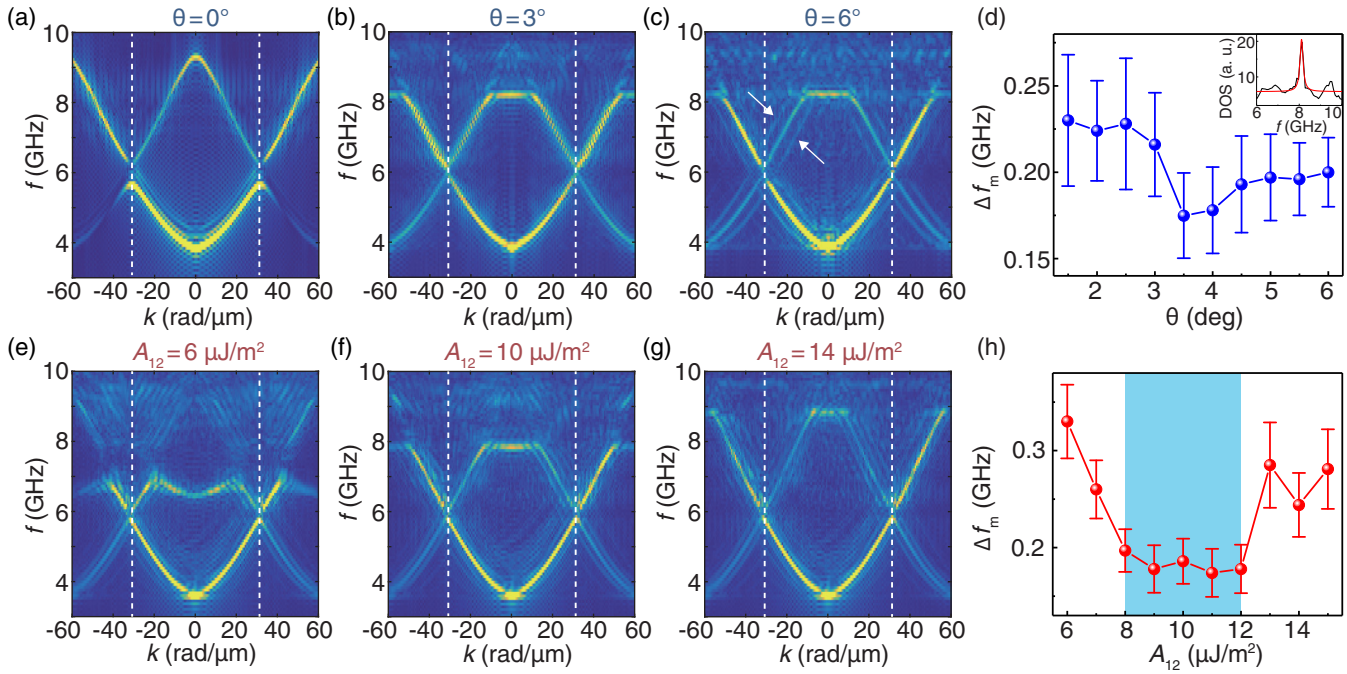

FIG. 2. (a) SW dispersion on commensurate bilayer magnonic crystal, i.e., with $\theta = 0^\circ$. (b) SW dispersion at the moiré unit cell center (*AB* stacking region) with $\theta = 3^\circ$. (c) SW dispersion at the moiré unit cell center (*AB* stacking region) with $\theta = 6^\circ$. White arrows indicate the side bands. The interlayer exchange coupling is fixed at $A_{12} = 11\ \mu\text{J/m}^2$ in (a)–(c). (d) Moiré flat-band bandwidth Δf_m as a function of twist angle θ. Δf_m is extrapolated from the linewidth of magnon density of states (DOS) around 8.2 GHz shown in the inset as an example at $\theta = 3.5^\circ$. (e)–(g) Simulated SW dispersion at the moiré unit cell center (*AB* stacking region) with a fixed twist angle $\theta = 3.5^\circ$ and alternating interlayer exchange coupling of (e) 6 $\mu\text{J/m}^2$, (f) 6 $\mu\text{J/m}^2$, and (g) 14 $\mu\text{J/m}^2$. (h) Interlayer exchange coupling dependence of moiré flat-band bandwidth Δf_m with $\theta = 3.5^\circ$. The light-blue shaded area highlights the region with high-quality moiré flat band.

(or Γ point) which is fundamentally different from its electronic [6] and photonic [14] counterparts as well as from the moiré 2D magnets [43,45], all of which exhibit a mini-flat-band around the *K* point in the band structure. The flat band in the magnetic moiré superlattice gives rise to zero magnon group velocity over a large wave vector range. As a result, a large number of magnons are "trapped" at the center of the moiré unit cell to form a magnonic nanocavity as shown in the spatial map of magnon intensity [Fig. 1(c)] with excitation at the flat-band frequency (8.2 GHz), where the white dashed square represents the same region as that in Fig. 1(a). A single spectrum of the magnon intensity extracted along the center of the localized magnon mode is presented in Fig. 1(d), where the calculated magnon intensity by Eq. (3) (red dashed curve) yields a linewidth of 185 nm. The linewidth can be roughly considered as the diameter of the magnonic nanocavity formed in the magnetic moiré superlattice. In addition to the strongly localized magnon mode, there appears also some weak propagating SWs, which could result from the nonzero magnon group velocity at the border of the flat band. Notably, the magnonic nanocavity studied in this work is localized at the *AB* stacking region [see Figs. 1(a) and 1(c)], which is different from those in the magic-angle graphene superlattices [6] and twisted bilayer photonic crystals [12], where the effect always occurs at the *AA* stacking region. In the magnetic moiré superlattice, it is observed around the *AA* stacking region where the flat band disappears in the magnon dispersion and SWs are found to propagate away (see Supplemental Material [62]).

In the following, we investigate the formation of the moiré flat band by tuning the twist angle θ and the interlayer exchange coupling A_{12}. At $\theta = 0$, the bilayer system is commensurate and its magnon dispersion resembles that for a single-layer magnonic crystal as shown in Fig. 2(a). If there is no interlayer exchange ($A_{12} = 0$) but only magnetic dipolar interaction between two layers, flat bands also cannot be formed (see Supplemental Material [62]), although one may observe some "side bands" [e.g., indicated by white arrows in Fig. 2(c)] in superposition to the conventional magnonic crystal band structure. Therefore, the twist angle θ and the interlayer exchange coupling A_{12} are two key ingredients to create moiré flat bands in a bilayer magnonic crystal system. We first fix the interlayer exchange coupling at $A_{12} = 11\ \mu\text{J/m}^2$ and vary the twist angle θ. Figures 2(a)–2(c) show three typical cases with different twist angles of $\theta = 0$, $\theta = 3^\circ$, and $\theta = 6^\circ$. In general, the magnonic flat band feature appears always around 8.2 GHz and survives within a relatively broad range of twist angles in stark contrast to electronic [6] and photonic [12] flat bands, which rely critically on the twist angle, i.e., the "magic angle." It is inferred that the frequency of the flat band in magnonic moiré superlattice is solely determined by the exchange coupling A_{12}. However, although the flat band is sustained at different angles, the quality of the flat band or its flatness relies rather critically

on the twist angle as shown in Fig. 2(d) with θ varying from 1.5° to 6°. The magnonic band flatness is characterized or defined as the linewidth of magnon density of state (DOS) around 8.2 GHz. The magnon DOS is calculated within the first BZ of the magnonic crystal and a Lorentz fitting is performed to obtain the moiré flat-band bandwidth Δf_{m}, as shown in the inset of Fig. 2(d). The minimum of Δf_{m} peaks around 3.5°, which can be considered as the "magic angle" to form the moiré magnonic flat band. By further increasing the twist angle, the side bands appear which reduce the flatness of the magnon band as shown in Fig. 2(d). In addition, by increasing the twist angle, the magnonic bandwidth decreases at the BZ boundaries, which is further discussed in the Supplemental Material [62]. Then, by fixing the twist angle at 3.5°, we vary the interlayer exchange coupling A_{12}. With $A_{12} = 6\ \mu\mathrm{J/m^2}$ [Fig. 2(e)], a curved magnon band appears around 6.8 GHz but the calculated moiré bandwidth Δf_{m} is quite large, i.e., does not exhibit good flatness. With a larger interlayer exchange $A_{12} = 10\ \mu\mathrm{J/m^2}$ [Fig. 2(f)], the curved magnon band becomes flat, and the frequency of the flat band rises to approximately 7.9 GHz. A mini-flat-band at the ground state (3.7 GHz) is also observed whose wave vector range corresponds approximately to $2\pi/a_{\mathrm{m}}$. The moiré flat band at 7.9 GHz is about 10 times broader covering more than half of the first magnonic BZ and reappears in the second magnonic BZ (around ± 60 rad/μm). By further increasing the interlayer exchange to $A_{12} = 14\ \mu\mathrm{J/m^2}$ [Fig. 2(g)], the moiré flat band shifts up in frequency to about 8.8 GHz with a much smaller wave vector range and deteriorated flatness. Magnonic band structures at more values of A_{12} are presented in the Supplemental Material [62], from which the moiré flat-band bandwidths are extrapolated and plotted in Fig. 2(h). The moiré flat band sustains a high-quality flatness (with $\Delta f_{\mathrm{m}} < 0.2$ GHz) over a relatively large range of A_{12} from $6\ \mu\mathrm{J/m^2}$ to $6\ \mu\mathrm{J/m^2}$ [yellow shaded area in Fig. 2(h)]. In general, we find the quality (flatness) of the moiré flat band is determined by the combination of the twist angle θ and interlayer exchange coupling A_{12}. For instance, the combination of $\theta = 3.5°$ and $A_{12} = 11\ \mu\mathrm{J/m^2}$ gives rise to an optimal moiré flat band as shown in Fig. 1(b). In other word, the "magic angle" to form the moiré flat band is closely associated with the interlayer exchange strength.

At an optimal combination of twist angle θ and interlayer exchange coupling A_{12}, a high-quality flat band is formed in the SW dispersion as shown in the inset of Fig. 3(a). We study and compare the flat-band mode (8.2 GHz; red arrow) and propagating mode (5 GHz; blue arrow) with a temporal excitation pulse as shown in Fig. 3(a) with 2 ns duration. The time-dependent magnetization dynamics m_{x} at the position of $x = 0$ is shown in Fig. 3(b) for excitation at 5 GHz and in Fig. 3(c) for excitation at 8.2 GHz (the flat-band frequency). In Fig. 3(b), the microwave pulse at 5 GHz is applied starting from 1 ns and instantly magnetization is found to oscillate with a reasonably large amplitude as shown in the blue curve. At the falling edge of the pulse (right edge of the yellow shaded area), the magnon spatial map [inset of Fig. 3(b)] reveals clear propagating SWs with a wavelength of approximately 300 nm that corresponds well with the wave vector at the blue arrow in the inset of Fig. 3(a). After the pulse is switched off, an abrupt decay of magnon intensity is observed

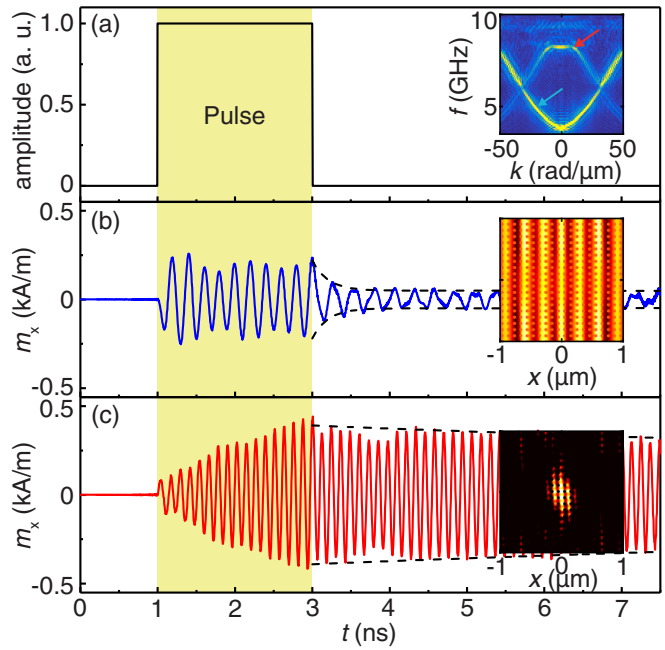

FIG. 3. (a) Microwave pulse applied in the bilayer magnetic moiré superlattice with duration of 2 ns. The inset shows SW dispersion at $\theta = 3.5°$ and $A_{12} = 11\ \mu\mathrm{J/m^2}$, where the red (blue) arrow indicates the flat-band mode at 8.2 GHz (a regular propagating mode at 5 GHz). (b) Time-domain magnetization dynamics m_{x} at 5 GHz in the center of a moiré unit cell (*AB* stacking region). The inset presents the magnon spatial distribution at the falling edge of the pulse (3 ns), where clear SW propagation is observed. The black dashed line is an exponential fit to the decay after the pulse is switched off. (c) Temporal magnetization oscillation at the flat-band frequency (8.2 GHz). The yellow shaded area suggests the pulse duration. The magnon intensity is found to increase with time within the pulse duration reaching a maximum at the pulse falling edge (3 ns), where the magnon spatial distribution is presented in the inset forming a magnonic nanocavity around the *AB* stacking region. The black line is an exponential fit to the decay after the pulse is switched off.

in Fig. 3(b). However, the remanent small amplitude can be sustained over a much longer timescale. Such phenomenon can be described by the following equation,

$$\mathcal{A}_{\mathrm{sw}} = C_1 \exp(-t/\tau_{\mathrm{m}}) + C_2 \exp(-t/\tau_0), \tag{1}$$

where $\mathcal{A}_{\mathrm{sw}}$ represents the SW amplitude, C_1 and C_2 are two time-independent prefactors, τ_{m} is the decay time for propagating magnon, and τ_0 is the decay time caused by the intrinsic damping of YIG, respectively. Due to lacking of localization for propagating SWs in Fig. 3(b), τ_{m} is found to be as small as 0.2 ns, yielding an effective cavity quality factor of $\mathcal{Q} = \omega\tau_{\mathrm{m}} = 6$, where ω is the angular frequency ($\omega = 2\pi f$). After 0.2 ns, the SW amplitude quickly relaxes to a more steady value and the frequency decreases to the ferromagnetic resonance 4 GHz. Then it would need much longer time to fully relax or damp to the equilibrium magnetization state corresponding to the magnetic damping of YIG $\tau_0 = 1/\alpha\omega$. Taking the intrinsic damping of YIG to be 1×10^{-4} [50,51],

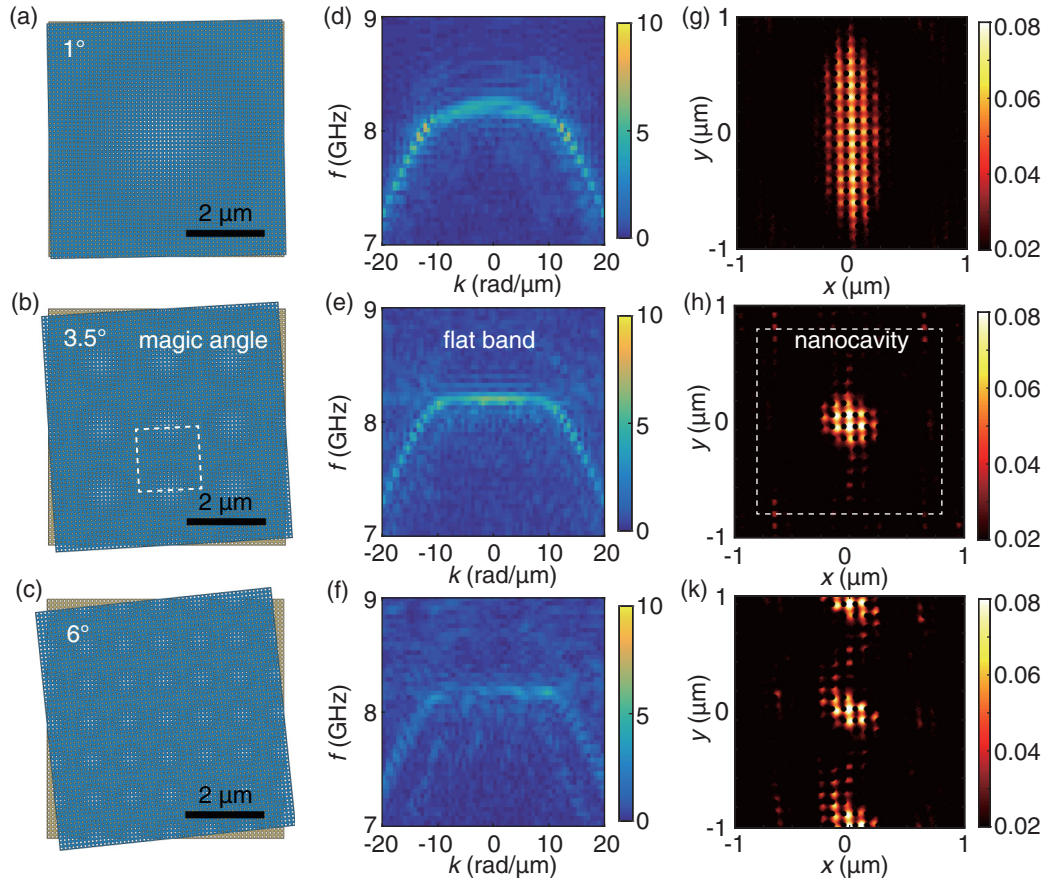

FIG. 4. (a)–(c) Schematic illustrations of twisted bilayer magnonic crystals with twist angles of (a) 1°, (b) 3.5°, and (c) 6°. The interlayer exchange coupling is fixed at 6 μJ/m^2. The white dashed square indicates a moiré unit cell with an area of 1.6 μm × 1.64 μm. (d)–(f) The SW dispersion near the flat-band region simulated at the center of the moiré unit cell for magnetic moiré superlattices with different twist angles of (d) 1°, (e) 3.5°, and (f) 6°. The excitation microwave power is set to be −30 dBm, smaller than that in Fig. 1. (g)–(k) Magnetization m_x snapshots of a 6 μm × 2 μm area at $t = 4.3$ ns after the start of continuous microwave excitation with twist angles of (g) 1°, (h) 3.5°, and (k) 6°.

one attains $\tau_0 = 398$ ns. Now if the excitation is made at the flat-band frequency being 8.2 GHz, the SW intensity accumulates within the pulse duration [Fig. 3(c)] and quickly surpasses that of the non-flat-band mode [Fig. 3(b)]. At the pulse falling edge (3 ns), the SW amplitude for the flat-band mode is more than double that for the non-flat-band mode. Moreover, a majority of the SW intensity is confined in a very small spatial region at the *AB* stacking area [inset of Fig. 3(c)]. For the flat-band mode at 8.2 GHz, the magnonic nanocavity is then formed due to the zero SW group velocity and a peak in magnon density state. By fitting the magnetization dynamics in Fig. 3(c) with Eq. (1), the magnon relaxation time $\tau_m = 20$ ns is obtained, leading to an effective quality factor $\mathcal{Q} = \omega\tau_m = 1030$. This high quality factor of the magnonic nanocavity is essential for the realization of highly localized magnon excitation for magnon Bose-Einstein condensation (BEC) [63–65] and even "magnon lasing" [66] in the future. The above described magic-angle magnonic nanocavity exhibits a distinctive feature: the confinement does not rely on a full forbidden band, but rather occurs at the flat band with a peak in magnon density of states. This confinement mechanism is fundamentally different from the nanocavity [67] or nanochannel [68] created by the defects within a conventional magnonic crystal, where the magnon confinement relies essentially on a full magnonic band gap. Given that there are no allowed states in the magnonic band gap, magnonic crystals act as a mirror (or a wall) to confine the defect magnon states. Contrary to Fig. 3(b), after the pulse is switched off, the magnon frequency is maintained at 8.2 GHz, not decreasing to 4 GHz. This intriguing feature implies that the localized magnons in the twisted bilayer mutually couple to form a self-oscillating hybridized mode at 8.2 GHz.

In Fig. 4, we further investigate the relation between the magnonic nanocavity and the formation of the magnon flat band in magnetic moiré superlattices with different twist angles. First of all, we find that to trigger the strong magnon confinement does not require high excitation power, so we lower the rf power from −10 dBm (Fig. 1) to −30 dBm (Fig. 4) in order to fully avoid the nonlinear spin precession in the system. The conversion between the microwave excitation field and the power is studied by the high-frequency structure simulator (see Supplemental Material [62]). Magnetic moiré superlattices with twist angles of $\theta = 1°$, 3.5°, and 6° are depicted in Figs. 4(a), 4(b) and 4(c) showing different moiré lattice constants of 5.6 μm, 1.6 μm, and 0.6 μm, respectively. The corresponding calculated magnon "flat-band"

dispersions at these three angles are shown in Figs. 4(d), 4(e) and 4(f). In general, the results of these three twist angles all exhibit a flat-band feature in the magnon dispersion, although with different "quality" or "flatness." The emergence of the magnon flat band over a relatively large range of twist angle offers much easier implementation of the magic-angle magnonic device in general applications than its counterpart in electronics, e.g., magic-angle bilayer graphene, which demands critically a small angle of a typical 1.1° [6]. The excitation at the magnon flat band increases the magnon DOS dramatically and creates strong magnon confinement at the center of a moiré unit cell (*AB* stacking region) as shown in Fig. 4(h) with a magic angle $\theta = 3.5°$. If the twist angle deviates from the optimal one (or magic angle), the flat band becomes not so "flat." With a small twist angle of 1°, the flat band is rounded up and shows a small "bump" around $k = 0$ [Fig. 4(d)], which eventually results in a poor magnon confinement at the moiré unit cell center as shown in Fig. 4(g). With a large twist angle of 6°, the magnon flat band appears to be disruptive, which projects into the real space as some "leakage" between two neighboring magnonic nanocavities. Therefore, for $A = 11\ \mu J/m^2$, the magnonic nanocavity with the optimal quality occurs at or around the "magic angle" of 3.5°.

Finally, we investigate the formation mechanism of the magnon flat bands and discuss the origin of the magic angle in magnetic moiré superlattices. We start with one single layer of magnonic crystal with square antidot lattices. Conventional magnonic band gaps are observed at magnonic BZ boundaries (see Supplemental Material [62]), very similar to those shown in Fig. 2(a) for a zero-twist-angle bilayer system. By twisting one single magnonic crystal layer with respect to the same SW wave vector k, we find the magnonic band shifts in both directions in the twisted layer (see Supplemental Material [62]), analogous to the side bands indicated by the white arrows in Fig. 2(c). If there is no interlayer exchange coupling (only interlayer dipolar interaction), three individual magnonic branches can be observed in the magnon dispersion without significant mode hybridization as illustrated in Fig. 5(a). The interlayer exchange coupling stimulates the strong interlayer magnon-magnon coupling [46–48], which manifests as the anticrossing between different magnonic branches, comparable to those observed in cavity magnonics [69] between magnons and cavity photons [70–73]. Therefore, the interlayer exchange coupling generates multiple anticrossings at the meeting points between three individual magnonic branches (one from the untwisted layer and two from the twisted layer), which eventually evolves to four quasi-flat-bands, two from the upper band (C1 and C2) and two from the lower band (V1 and V2), as shown in Fig. 5(b). Microscopically, the effective interlayer exchange interaction considering its integration in the whole moiré superlattice is crucially dependent on the interlayer stacking configurations and preserves moiré translational symmetry as $A_{12}(r) = A_{12}(r + R)$, where r is the position within the moiré supercell, and R is a moiré superlattice vector. The origin of flat bands in magic-angle twisted bilayer graphene is different from the magnonic flat bands. The flatness in magic-angle twisted bilayer graphene has a topological origin with nonvanishing Chern numbers and is reminiscent of pseudo-Landau-levels

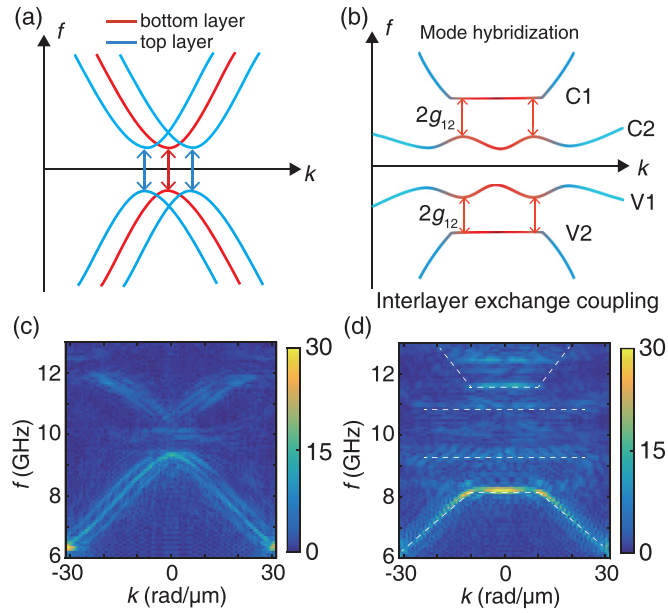

FIG. 5. (a) Sketch of uncoupled magnetic moiré superlattice with shifted bands in the wave vector space. The red (blue) curve indicates the magnonic bands of the bottom (top) layer magnonic crystal. The bottom layer is aligned with the antenna, whereas the top layer is rotated with respect to the bottom layer as shown in Fig. 4. The arrows mark the band gap of the magnonic crystals. (b) With strong interlayer exchange coupling, the magnon branches start to hybridize and form several flat bands due to the mode anticrossings. Four quasi-flat-bands are labeled as C1, C2, V1, and V2. Red arrows indicate the new gaps induced by the mode hybridization, which is about twice the magnon-magnon coupling strength g_{12}. (c) A zoom-in simulated magnonic band structure near the band gap in the absence of the interlayer exchange coupling. (d) Simulation results on magnonic band structure near the band gap with $A_{12} = 11\ \mu J/m^2$. The twist angle is fixed at $\theta = 3.5°$. Four quasi-flat-bands are marked by white dashed lines.

[74,75], which emerge from the coupling between Dirac fermions of graphene with the pseudo-magnetic-fields generated by the spatial varying interlayer hopping term. For the magic-angle magnonic nanocavity studied in this work, the flat bands observed in Fig. 5(b) and Fig. 2 originate from the lowest quasi-flat-band V2 [74] as shown in Fig. 5. Prior to the mode hybridization, the magnonic crystals provide large magnon band gaps, and consequently after mode hybridization the quasi-flat-bands C2 and V1 are still far apart in frequency and cannot be unified to one flat mode. Nevertheless, all four quasi-flat-bands can be vaguely observed in the Fig. 5(d) with the lowest mode V2 being the strongest, which is essentially the flat band we discuss in this work. Thus, one key element to form the flat bands apart from the magic angle is the interlayer exchange coupling. The role of the interlayer exchange coupling in magnonic magic-angle systems is comparable to the interlayer separation in its photonic [12] counterparts. The interlayer magnon-magnon coupling strength (g_{12}) manifests itself as the anticrossing gap ($2g_{12}$) between the magnon branches of the upper and lower layers and is given rise by the interlayer-exchange-induced [46–48]

magnon spin torque [76–79] τ_{12}^{m}, which is proportional to the effective interlayer exchange field $\mathbf{h}_{\mathrm{eff}} = A_{12}|\nabla_z \mathbf{m}|^2$. Then we obtain

$$g_{12} \propto \tau_{12}^{\mathrm{m}} = \mathrm{m} \times A_{12} \frac{\partial^2 \mathrm{m}}{\partial z^2}. \tag{2}$$

Equation (2) suggests that the magnetization gradient in the z direction is required to generate a strong interlayer magnon-magnon coupling in order to form the magnon flat bands. At the edge of the moiré lattice, namely the *AA* region, the magnonic crystal lattices of two layers are overlapped (see Supplemental Material for magnetic texture distributions [62]), and thus the magnetic texture gradient is minimized, which results in a weak interlayer magnon-magnon coupling [46]. At the center of the moiré lattice (the *AB* region), however, the magnetic texture difference between the two layers is maximized, and thus the interlayer exchange becomes most effective to provide strong magnon-magnon coupling similar to the case of exchange springs [46,80], and can eventually generate flat bands as shown in Fig. 5. This explains why the magnonic nanocavities occur always at the *AB* region different from the photonic nanocavities [14] at the *AA* region due to the nature of the exchange interaction. In this work, we focus on the low-frequency flat bands which are due to the magnon-magnon mode hybridization. It is shown that for magnon-photon hybridization, the topological Chern number of the coupled wave becomes quantized into nonzero integers [81]. The effect of topology on the magnonic flat bands in the magnetic moiré superlattice requires further investigation.

The flat band provides a high magnon DOS, i.e., a wide range of wave vector distribution Δk_0 at a given magnon frequency. In analog to the magic-angle photonic nanocavities [14], such high DOS is a key to generate the highly confined mode. The spatial distribution of the magnon intensity $I_0(x)$ for the magic-angle magnonic nanocavity induced by the magnon flat band can be calculated by the summation or superposition of all SW modes (or states) at the one-and-the-same flat-band frequency ω_0. After taking approximation of continuous k variation (see Supplemental Material [62]) in magnon dispersion, one derives

$$I_0(x) = \frac{A^2 S}{\pi^2} \left| \frac{\sin\left(\frac{1}{2}\Delta k_0 x\right)}{x} \right|^2, \tag{3}$$

where A is the SW amplitude assumed to be constant for all modes at the flat band. S stands for the area of one moiré unit cell. By taking the flat-band wave vector bandwidth $\Delta k_0 \approx 30\ \mathrm{rad}/\mu\mathrm{m}$ extracted from results in Fig. 1(b), one can calculate the magnon intensity distribution $I_0(x)$ based on Eq. (3) with a spatial linewidth $\Delta x_0 = 185$ nm, which is comparable with the intensity distribution attained from simulation results in Fig. 1(d).

III. CONCLUSIONS AND OUTLOOK

To conclude, we have investigated the moiré magnetic superlattices with a twist angle using micromagnetic simulations. The results show the emergence of magnon flat bands in the magnon dispersion, which eventually results in a magnonic nanocavity with a diameter of about 185 nm. The flatness of the flat band and also the quality of the magnonic nanocavity is found to be highly tunable with two major physical quantities, i.e., the twist angle θ and the interlayer exchange A_{12}. The ideal flat band is achieved with the combination of the "magic angle" $\theta = 3.5^\circ$ and interlayer exchange $A_{12} = 11\ \mu\mathrm{J/m}^2$ with reasonably good tolerance with the deviation from the optimal values. The results on the pulse simulation demonstrate that the magic-angle magnonic nanocavity with a high quality factor enables a strong enhancement or accumulation of magnon intensity inside the nanocavity, which provides great perspectives to achieve magnon BEC in the moiré magnetic superlattices and to pave the way toward "magnon lasing" with high intensities. The magnonic flat band observed in this work is found to be easily tunable with an applied magnetic field as shown in the Supplemental Material [62], which enables the excitation of the magic-angle magnonic nanocavity at different demanded frequencies. This field-tunability of flat bands may be obvious for the magic-angle magnetic systems, but nontrivial for its electronic and photonic counterparts.

Finally, the formation of the magnon flat band is attributed to the mode anticrossings in the magnon dispersion induced by interlayer magnon-magnon coupling. To generate experimentally the magnon flat band and realize the magic-angle magnonic nanocavity based on this artificial crystal with a periodicity on a 100 nm scale, we showed that we could adopt the simplified nanolithography technique as used in moiré photonic nanocavity [14] where the effective exchange coupling is fixed and the twist angle is the only tuning parameter. By introducing a nonmagnetic spacer between two magnonic-crystal stacks, one can tune the interlayer exchange by the thickness of the spacer with high sensitivity ruled by the RKKY interaction [82]. Recent demonstrations on tunable magnon-magnon coupling [83] in synthetic antiferromagnets may also provide an experimental approach to control the coupling strength. The nature of the interlayer exchange coupling explains the magnon confinement at the *AB* stacking region of the moiré magnetic superlattices, which is fundamentally different from the magic-angle photonic nanocavity always at the *AA* region. The theoretical calculation indicates that broader flat band may introduce a even more focused magnonic nanocavity, to be studied and achieved in experiments in the future. Last but not least, our studies also contribute to the emerging field of three-dimensional (3D) magnonics [84,85], where magnon propagation properties are modulated by the vertical interlayer coupling [86,87] enabling the transition from 2D to 3D magnonic architectures.

ACKNOWLEDGMENTS

The authors acknowledge support from the NSF China under Grants No. 12074026, No. 12104208, and No. U1801661, the 111 Talent Program B16001, and the National Key Research and Development Program of China, Grants No. 2016YFA0300802 and No. 2017YFA0206200.

[1] E. Suárez Morell, J. D. Correa, P. Vargas, M. Pacheco, and Z. Barticevic, Flat bands in slightly twisted bilayer graphene: Tight-binding calculations, Phys. Rev. B **82**, 121407(R) (2010).

[2] R. Bistritzer and A. H. MacDonald, Unconventional superconductivity in magic-angle graphene superlattices, Proc. Natl. Acad. Sci. U.S.A. **108**, 12233 (2011).

[3] Q. Tong, H. Yu, Q. Zhu, Y. Wang, X. Xu, and W. Yao, Topological mosaics in moiré superlattices of van der Waals heterobilayers, Nat. Phys. **13**, 356 (2017).

[4] K. Kim, A. DaSilva, S. Huang, B. Fallahazad, S. Larentis, T. Taniguchi, K. Watanabe, B. J. LeRoy, A. H. MacDonald, and E. Tutuc, Tunable moiré bands and strong correlations in small-twist-angle bilayer graphene, Proc. Natl. Acad. Sci. U.S.A. **114**, 3364 (2017).

[5] Y. Cao, V. Fatemi, A. Demir, S. Fang, S. L. Tomarken, J. Y. Luo, J. D. Sanchez-Yamagishi, K. Watanabe, T. Taniguchi, E. Kaxiras, R. C. Ashoori, and P. Jarillo-Herrero, Correlated insulator behaviour at half-filling in magic-angle graphene superlattices, Nature (London) **556**, 80 (2018).

[6] Y. Cao, V. Fatemi, S. Fang, K. Watanabe, T. Taniguchi, E. Kaxiras, and P. Jarillo-Herrero, Unconventional superconductivity in magic-angle graphene superlattices, Nature (London) **556**, 43 (2018).

[7] X. Lu, P. Stepanov, W. Yang, M. Xie, M. A. Aamir, I. Das, C. Urgell, K. Watanabe, T. Taniguchi, G. Zhang, A. Bachtold, A. H. MacDonald, and D. K. Efetov, Superconductors, orbital magnets and correlated states in magic-angle bilayer graphene, Nature (London) **574**, 653 (2019).

[8] F. Wu, A. H. MacDonald, and I. Martin, Theory of Phonon-Mediated Superconductivity in Twisted Bilayer Graphene, Phys. Rev. Lett. **121**, 257001 (2018).

[9] T. J. Peltonen, R. Ojajärvi, and T. T. Heikkilä, Theory of phonon-mediated superconductivity in twisted bilayer graphene, Phys. Rev. B **98**, 220504(R) (2018).

[10] M. Yankowitz, S. Chen, H. Polshyn, Y. Zhang, K. Watanabe, T. Taniguchi, D. Graf, A. F. Young, and C. R. Dean, Tuning superconductivity in twisted bilayer graphene, Science **363**, 1059 (2019).

[11] X. Zhang, K.-T. Tsai, Z. Zhu, W. Ren, Y. Luo, S. Carr, M. Luskin, E. Kaxiras, and K. Wang, Correlated Insulating States and Transport Signature of Superconductivity in Twisted Trilayer Graphene Superlattices, Phys. Rev. Lett. **127**, 166802 (2021).

[12] K. Dong, T. Zhang, J. Li, Q. Wang, F. Yang, Y. Rho, D. Wang, C. P. Grigoropoulos, J. Wu, and J. Yao, Flat Bands in Magic-Angle Bilayer Photonic Crystals at Small Twists, Phys. Rev. Lett. **126**, 223601 (2021).

[13] B. Lou, N. Zhao, M. Minkov, C. Guo, M. Orenstein, and S. Fan, Theory for Twisted Bilayer Photonic Crystal Slabs, Phys. Rev. Lett. **126**, 136101 (2021).

[14] X.-R. Mao, Z.-K. Shao, H.-Y. Luan, S.-L. Wang, and R.-M. Ma, Magic-angle lasers in nanostructured moiré superlattice, Nat. Nanotechnol. **16**, 1099 (2021).

[15] V. Vlaminck, and M. Bailleul, Current-induced spin-wave Doppler shift, Science **322**, 410 (2008).

[16] Y. Kajiwara, K. Harii, S. Takahashi, J. Ohe, K. Uchida, M. Mizuguchi, H. Umezawa, H. Kawai, K. Ando, K. Takanashi, S. Maekawa, and E. Saitoh, Transmission of electrical signals by spin-wave interconversion in a magnetic insulator, Nature (London) **464**, 262 (2010).

[17] V. V. Kruglyak, S. O. Demokrotiv, and D. Grundler, Magnonics, J. Phys. D: Appl. Phys. **43**, 264001 (2010).

[18] A. V. Chumak, V. I. Vasyuchka, A. A. Serga, and B. Hillebrands, Magnon spintronics, Nat. Phys. **11**, 453 (2015).

[19] L. J. Cornelissen, J. Liu, R. A. Duine, J. B. Youssef, and B. J. van Wees, Long-distance transport of magnon spin information in a magnetic insulator at room temperature, Nat. Phys. **11**, 1022 (2015).

[20] A. Haldar, D. Kumar, and A. O. Adeyeye, A reconfigurable waveguide for energy-efficient transmission and local manipulation of information in a nanomagnetic device, Nat. Nanotechnol. **11**, 437 (2016).

[21] H. Yu, J. Xiao, and H. Schultheiss, Magnetic texture based magnonics, Phys. Rep. **905**, 1 (2021).

[22] P. Pirro, V. I. Vasyuchka, A. A. Serga, and B. Hillebrands, Advances in coherent magnonics, Nat. Rev. Mater. **6**, 1114 (2021).

[23] A. Khitun, M. Bao, and K. L. Wang, Magnonic logic circuits, J. Phys. D: Appl. Phys. **43**, 264005 (2010).

[24] G. Csaba, A. Papp, and W. Porod, Perspectives of using spin waves for computing and signal processing, Phys. Lett. A **381**, 1471 (2017).

[25] S. Neusser, G. Durr, H. G. Bauer, S. Tacchi, M. Madami, G. Woltersdorf, G. Gubbiotti, C. H. Back, and D. Grundler, Anisotropic Propagation and Damping of Spin Waves in a Nanopatterned Antidot Lattice, Phys. Rev. Lett. **105**, 067208 (2010).

[26] J. Ding, M. Kostylev, and A. O. Adeyeye, Magnonic Crystal as a Medium with Tunable Disorder on a Periodical Lattice, Phys. Rev. Lett. **107**, 047205 (2011).

[27] G. Gubbiotti, S. Tacchi, M. Madami, G. Carlotti, S. Jain, A. O. Adeyeye, and M. P. Kostylev, Collective spin waves in a bicomponent two-dimensional magnonic crystal, Appl. Phys. Lett. **100**, 162407 (2012).

[28] M. Krawczyk and D. Grundler, Review and prospects of magnonic crystals and devices with reprogrammable band structure, J. Phys.: Condens. Matter **26**, 123202 (2014).

[29] S. Tacchi, G. Gubbiotti, M. Madami, and G. Carlotti, Brillouin light scattering studies of 2D magnonic crystals, J. Phys.: Condens. Matter **29**, 073001 (2017).

[30] S. A. Díaz, T. Hirosawa, J. Klinovaja, and D. Loss, Chiral magnonic edge states in ferromagnetic skyrmion crystals controlled by magnetic fields, Phys. Rev. Research **2**, 013231 (2020).

[31] S. Tacchi, F. Montoncello, M. Madami, G. Gubbiotti, G. Carlotti, L. Giovannini, R. Zivieri, F. Nizzoli, S. Jain, A. O. Adeyeye, and N. Singh, Band Diagram of Spin Waves in a Two-Dimensional Magnonic Crystal, Phys. Rev. Lett. **107**, 127204 (2011).

[32] S. Tacchi, G. Duerr, J. W. Klos, M. Madami, S. Neusser, G. Gubbiotti, G. Carlotti, M. Krawczyk, and D. Grundler, Forbidden Band Gaps in the Spin-Wave Spectrum of a Two-Dimensional Bicomponent Magnonic Crystal, Phys. Rev. Lett. **109**, 137202 (2012).

[33] J. Topp, D. Heitmann, M. P. Kostylev, and D. Grundler, Making a Reconfigurable Artificial Crystal by Ordering Bistable Magnetic Nanowires, Phys. Rev. Lett. **104**, 207205 (2010).

[34] Q. Wang, A. V. Chumak, L. Jin, H. Zhang, B. Hillebrands, and Z. Zhong, Making a reconfigurable artificial crystal by ordering bistable magnetic nanowires, Phys. Rev. B **95**, 134433 (2017).

[35] A. K. Mondal, C. Banerjee, A. Adhikari, A. K. Chaurasiya, S. Choudhury, J. Sinha, S. Barman, and A. Barman, Spin-texture driven reconfigurable magnonics in chains of connected $Ni_{80}Fe_{20}$ submicron dots, Phys. Rev. B **101**, 224426 (2020).

[36] M. Mruczkiewicz, M. Krawczyk, G. Gubbiotti, S. Tacchi, Y. A. Filimonov, D. V. Kalyabin, I. V. Lisenkov, and S. A. Nikitov, Nonreciprocity of spin waves in metallized magnonic crystal, New J. Phys. **15**, 113023 (2013).

[37] O. Gladii, M. Haidar, Y. Henry, M. Kostylev, and M. Bailleul, Frequency nonreciprocity of surface spin wave in permalloy thin films, Phys. Rev. B **93**, 054430 (2016).

[38] J. Chen, T. Yu, C. Liu, T. Liu, M. Madami, K. Shen, J. Zhang, S. Tu, M. S. Alam, K. Xia, M. Wu, G. Gubbiotti, Y. M. Blanter, G. E. W. Bauer, and H. Yu, Excitation of unidirectional exchange spin waves by a nanoscale magnetic grating, Phys. Rev. B **100**, 104427 (2019).

[39] J. Chen, H. Yu, and G. Gubbiotti, Unidirectional spin-wave propagation and devices, J. Phys. D: Appl. Phys. **55**, 123001 (2022).

[40] R. A. Gallardo, D. Cortés-Ortuño, T. Schneider, A. Roldán-Molina, F. Ma, R. E. Troncoso, K. Lenz, H. Fangohr, J. Lindner, and P. Landeros, Flat Bands, Indirect Gaps, and Unconventional Spin-Wave Behavior Induced by a Periodic Dzyaloshinskii-Moriya Interaction, Phys. Rev. Lett. **122**, 067204 (2019).

[41] X. Ma, G. Yu, C. Tang, X. Li, C. He, J. Shi, K. L. Wang, and X. Li, Interfacial Dzyaloshinskii-Moriya Interaction: Effect of 5*d* Band Filling and Correlation with Spin Mixing Conductance, Phys. Rev. Lett. **120**, 157204 (2018).

[42] Y. Sun, H. Chang, M. Kabatek, Y. Y. Song, Z. Wang, M. Jantz, W. Schneider, M. Wu, E. Montoya, B. Kardasz, B. Heinrich, S. G. E. te Velthuis, H. Schultheiss, and A. Hoffmann, Damping in Yttrium Iron Garnet Nanoscale Films Capped by Platinum, Phys. Rev. Lett. **111**, 106601 (2013).

[43] Y.-H. Li and R. Cheng, Moiré magnons in twisted bilayer magnets with collinear order, Phys. Rev. B **102**, 094404 (2020).

[44] D. Ghader, Magnon magic angles and tunable Hall conductivity in 2D twisted ferromagnetic bilayers, Sci. Rep. **10**, 15069 (2020).

[45] C. Wang, Y. Gao, H. Lv, X. Xu, and D. Xiao, Stacking Domain Wall Magnons in Twisted van der Waals Magnets, Phys. Rev. Lett. **125**, 247201 (2020).

[46] S. Klingler, V. Amin, S. Geprägs, K. Ganzhorn, H. Maier-Flaig, M. Althammer, H. Huebl, R. Gross, R. D. McMichael, M. D. Stiles, S. T. B. Goennenwein, and M. Weiler, Spin-Torque Excitation of Perpendicular Standing Spin Waves, Phys. Rev. Lett. **120**, 127201 (2018).

[47] J. Chen, C. Liu, T. Liu, Y. Xiao, K. Xia, G. E. W. Bauer, M. Wu, and H. Yu, Strong Interlayer Magnon-Magnon Coupling in Magnetic Metal-Insulator Hybrid Nanostructures, Phys. Rev. Lett. **120**, 217202 (2018).

[48] H. Qin, S. J. Hämäläinen, and S. van Dijken, Exchange-torque-induced excitation of perpendicular standing spin waves in nanometer-thick YIG films, Sci. Rep. **8**, 5755 (2018).

[49] Y. Li, W. Cao, V. P. Amin, Z. Zhang, J. Gibbons, J. Sklenar, J. Pearson, P. M. Haney, M. D. Stiles, W. E. Bailey, V. Novosad, A. Hoffmann, and W. Zhang, Coherent Spin Pumping in a Strongly Coupled Magnon-Magnon Hybrid System, Phys. Rev. Lett. **124**, 117202 (2020).

[50] H. Chang, P. Li, W. Zhang, T. Liu, A. Hoffmann, L. Deng, and M. Wu, Nanometer-thick yttrium iron garnet films with extremely low damping, IEEE Magn. Lett. **5**, 6700 (2014).

[51] H. Yu, O. Allivy Kelly, V. Cros, R. Bernard, P. Bortolotti, A. Anane, F. Brandl, R. Huber, I. Stasinopoulos, and D. Grundler, Magnetic thin-film insulator with ultra-low spin wave damping for coherent nanomagnonics, Sci. Rep. **4**, 6848 (2015).

[52] M. Wu, A. Hoffmann, R. E. Camley, and R. L. Stamps, *Solid State Physics: Recent Advances in Magnetic Insulators from Spintronics to Microwave Applications* (Academic Press, New York, 2013), Vol. 64.

[53] S. Watanabe, V. S. Bhat, K. Baumgaertl, and D. Grundler, Direct observation of worm-like nanochannels and emergent magnon motifs in artificial ferromagnetic quasicrystals, Adv. Funct. Mater. **30**, 2001388 (2020).

[54] F. Ciubotaru, T. Devolder, M. Manfrini, C. Adelmann, and I. P. Radu, All electrical propagating spin wave spectroscopy with broadband wavevector capability, Appl. Phys. Lett. **109**, 012403 (2016).

[55] J. R. Eshbach and R. W. Damon, Surface magnetostatic modes and surface spin waves, Phys. Rev. **118**, 1208 (1960).

[56] K. Yamamoto, G. C. Thiang, P. Pirro, K.-W. Kim, K. Everschor-Sitte, and E. Saitoh, Topological Characterization of Classical Waves: The Topological Origin of Magnetostatic Surface Spin Waves, Phys. Rev. Lett. **122**, 217201 (2019).

[57] A. Fert, Nobel Lecture: Origin, development, and future of spintronics, Rev. Mod. Phys. **80**, 1517 (2008).

[58] S. O. Demokritov, C. Bayer, S. Poppe, M. Rickart, J. Fassbender, B. Hillebrands, D. I. Kholin, N. M. Kreines, and O. M. Liedke, Control of Interlayer Exchange Coupling in Fe/Cr/Fe Trilayers by Ion Beam Irradiation, Phys. Rev. Lett. **90**, 097201 (2003).

[59] Y. Fan, P. Quarterman, J. Finley, J. Han, P. Zhang, J. T. Hou, M. D. Stiles, A. J. Grutter, and L. Liu, Manipulation of Coupling and Magnon Transport in Magnetic Metal-Insulator Hybrid Structures, Phys. Rev. Appl. **13**, 061002(R) (2020).

[60] H. Wu, L. Huang, C. Fang, B. S. Yang, C. H. Wan, G. Q. Yu, J. F. Feng, H. X. Wei, and X. F. Han, Magnon Valve Effect between Two Magnetic Insulators, Phys. Rev. Lett. **120**, 097205 (2018).

[61] M. Donahue and D. Porter, OOMMF User's Guide, Version 1.0, National Institute of Standards and Technology, Gaithersburg, MD, Interagency Report NISTIR 6376 Edition, September 1999, http://math.nist.gov/oommf.

[62] See Supplemental Material at http://link.aps.org/supplemental/10.1103/PhysRevB.105.094445 for magnonic band structures of single-layer magnonic crystals and uncoupled magnetic moiré superlattices, magnonic band structure of the *AA* stacking region, magnonic band structures at more values of A_{12}, power dependence of the magnonic nanocavity induced by flat bands, high-frequency structure simulator of the excitation antenna, magnetization texture distributions at different regions in the moiré superlattice, magnon intensity for the magic-angle magnonic nanocavity, and tuning of flat-band frequency by external magnetic fields.

[63] S. O. Demokritov, V. E. Demidov, O. Dzyapko, G. A. Melkov, A. A. Serga, B. Hillebrands, and A. N. Slavin, Bose-Einstein condensation of quasi-equilibrium magnons at room temperature under pumping, Nature (London) **443**, 430 (2006).

[64] T. Giamarchi, C. Rüegg, and O. Tchernyshyov, Bose-Einstein condensation in magnetic insulators, Nat. Phys. **4**, 198 (2008).

[65] M. Schneider, T. Brächer, D. Breitbach, V. Lauer, P. Pirro, D. A. Bozhko, H. Yu. Musiienko-Shmarova, B. Heinz, Q. Wang, T. Meyer *et al.*, Bose-Einstein condensation of quasiparticles by rapid cooling, Nat. Nanotechnol. **15**, 457 (2020).

[66] L. Berger, Multilayers as spin-wave emitting diodes, J. Appl. Phys. **81**, 4880 (1997).

[67] N. Kumar, and A. Prabhakar, Resonant spin wave excitations in a magnonic crystal cavity, J. Magn. Magn. Mater. **450**, 46 (2018).

[68] T. Schwarze and D. Grundler, Magnonic crystal wave guide with large spin wave propagation velocity in CoFeB, Appl. Phys. Lett. **102**, 222412 (2013).

[69] B. Z. Rameshti, S. V. Kusminskiy, J. A. Haigh, K. Usami, D. Lachance-Quirion, Y. Nakamura, C.-M. Hu, H. X. Tang, G. E. W. Bauer, and Y. M. Blanter, Cavity magnonics, arXiv:2106.09312.

[70] H. Huebl, C. W. Zollitsch, J. Lotze, F. Hocke, M. Greifenstein, A. Marx, R. Gross, and S. T. B. Goennenwein, High Cooperativity in Coupled Microwave Resonator Ferrimagnetic Insulator Hybrids, Phys. Rev. Lett. **111**, 127003 (2013).

[71] X. Zhang, C.-L. Zou, L. Jiang, and H. X. Tang, Strongly Coupled Magnons and Cavity Microwave Photons, Phys. Rev. Lett. **113**, 156401 (2014).

[72] L. Bai, M. Harder, Y. P. Chen, X. Fan, J. Q. Xiao, and C.-M. Hu, Spin Pumping in Electrodynamically Coupled Magnon-Photon Systems, Phys. Rev. Lett. **114**, 227201 (2015).

[73] Y. Cao, P. Yan, H. Huebl, S. T. B. Goennenwein, and G. E. W. Bauer, Exchange magnon-polaritons in microwave cavities, Phys. Rev. B **91**, 094423 (2015).

[74] G. Tarnopolsky, A. J. Kruchkov, and A. Vishwanath, Origin of Magic Angles in Twisted Bilayer Graphene, Phys. Rev. Lett. **122**, 106405 (2019).

[75] J. Liu, J. Liu, and X. Dai, Pseudo Landau level representation of twisted bilayer graphene: Band topology and implications on the correlated insulating phase, Phys. Rev. B **99**, 155415 (2019).

[76] J. C. Slonczewski, Initiation of spin-transfer torque by thermal transport from magnons, Phys. Rev. B **82**, 054403 (2010).

[77] P. Yan, X. S. Wang, and X. R. Wang, All-Magnonic Spin-Transfer Torque and Domain Wall Propagation, Phys. Rev. Lett. **107**, 177207 (2011).

[78] J. Han, P. Zhang, J. T. Hou, S. A. Siddiqui, and L. Liu, Mutual control of coherent spin waves and magnetic domain walls in a magnonic device, Science **366**, 1121 (2019).

[79] Y. Wang, D. Zhu, Y. Yang, K. Lee, R. Mishra, G. Go, S.-H. Oh, K. Cai, E. Liu, S. D. Pollard *et al.*, Magnetization switching by magnon-mediated spin torque through an antiferromagnetic insulator, Science **366**, 1125 (2019).

[80] K. L. Livesey, D. C. Crew, and R. L. Stamps, Spin wave valve in an exchange spring bilayer, Phys. Rev. B **73**, 184432 (2006).

[81] A. Okamoto, R. Shindou, and S. Murakami, Berry curvature for coupled waves of magnons and electromagnetic waves, Phys. Rev. B **102**, 064419 (2020).

[82] S. S. P. Parkin, R. Bhadra, and K. P. Roche, Oscillatory Magnetic Exchange Coupling through Thin Copper Layers, Phys. Rev. Lett. **66**, 2152 (1991).

[83] Y. Shiota, T. Taniguchi, M. Ishibashi, T. Moriyama, and T. Ono, Tunable Magnon-Magnon Coupling Mediated by Dynamic Dipolar Interaction in Synthetic Antiferromagnets, Phys. Rev. Lett. **125**, 017203 (2020).

[84] G. Gubbiotti, T. Taniguchi, M. Ishibashi, T. Moriyama, and T. Ono, *Three-Dimensional Magnonics* (Jenny Stanford, Singapore, 2019).

[85] A. Barman, G. Gubbiotti, S. Ladak, A. O. Adeyeye, M. Krawczyk, J. Gräfe, C. Adelmann, S. Cotofana, A. Naeemi, V. I. Vasyuchka *et al.*, The 2021 magnonics roadmap, J. Phys.: Condens. Matter **33**, 413001 (2021).

[86] G. Gubbiotti, X. Zhou, Z. Haghshenasfard, M. G. Cottam, and A. O. Adeyeye, Reprogrammable magnonic band structure of layered permalloy/Cu/permalloy nanowires, Phys. Rev. B **97**, 134428 (2018).

[87] P. Graczyk, M. Krawczyk, S. Dhuey, W.-G. Yang, H. Schmidt, and G. Gubbiotti, Magnonic band gap and mode hybridization in continuous permalloy films induced by vertical dynamic coupling with an array of permalloy ellipses, Phys. Rev. B **98**, 174420 (2018).